Journal of Wind Engineering & Industrial Aerodynamics 277 (2026) 106578

Contents lists available at ScienceDirect

Journal of Wind Engineering & Industrial Aerodynamics

journal homepage: www.elsevier.com/locate/jweia

Wind-tunnel characterisation of road-vehicles in crosswind conditions ☆

Carlos Esteban Araya Reyes *, Irene Lechiguero Pardo, Stefano Negri, Gisella Tomasini

Department of Mechanical Engineering, Politecnico di Milano, Via La Masa 1, 20156 Milano, Italy

ARTICLE INFO

Keywords:
Crosswind
Wind tunnel
Vehicle aerodynamics
Vehicle stability
Road vehicles

ABSTRACT

Assessing the aerodynamic response of road vehicles under crosswind conditions is essential for understanding vehicle stability and safety. Such assessments require reliable aerodynamic data; however, much of the existing literature is based on experiments performed under disparate conditions or limited yaw-angle ranges. As a result, consistent and comparable reference datasets spanning multiple road-vehicle classes remain scarce. The present paper provides a consistent set of aerodynamic coefficients for the six load components (longitudinal, lateral and vertical forces; roll, pitch and yaw moments) for four vehicle classes: a saloon car (DrivAer geometry), a small lorry, a double-decker coach and an articulated lorry. The experimental campaign was conducted on reduced geometric scale models in the low-turbulence test section of the Politecnico di Milano wind tunnel under uniform flat-ground conditions, covering wind-yaw angles from 0° to 180°. The results show a strong dependence of crosswind aerodynamics on vehicle geometry, with pronounced differences between low-profile and high-sided vehicles. High-sided vehicles develop substantially larger lateral-force and rolling-moment coefficients, reaching up to approximately thirty times the saloon-car values when the double-decker coach or the trailer unit of the articulated lorry is considered. For the saloon car, a dependence of the aerodynamic loads on wind speed is observed. Abrupt changes in side-force and rolling-moment trends occur at specific yaw angles for smoother geometries, whereas sharp-edged configurations (small lorry and articulated trailer) exhibit smoother and more continuous behaviour. Overall, the results provide a coherent dataset for benchmarking, CFD validation and crosswind-stability studies across diverse road-vehicle classes.

1. Introduction

Road transport is fundamental to mobility, economic activity and public safety, and its reliable operation under adverse conditions is therefore essential. The increasing frequency and intensity of extreme weather events associated with climate change are creating growing challenges for the safety and functionality of road networks. In this context, enhancing the resilience of road transport systems has become a key priority. Among climate-related hazards, severe wind events are particularly critical, as they can induce significant transient loads on vehicles, adversely affecting stability (Markolf et al., 2019; Ji et al., 2022).

With storm activity rising across northern and central Europe (European Environment Agency, 2024), and similar trends reported in North America (Deehan et al., 2025) and Asia (Intergovernmental Panel on Climate Change, 2023), the frequency and intensity of windstorms are becoming an ever more pressing concern. For ground transportation systems that are inherently exposed to wind, these events may represent significant risks. In road vehicles crosswind may increase the risk of lateral displacement, loss of control or even may lead the vehicle to rollover (Coleman and Baker, 1990, 1994). In fact, studies have shown a strong correlation between storm events and vehicle accidents (Baker and Reynolds, 1991; Becker et al., 2022).

In other transportation sectors, such as railways, crosswind effects have been extensively investigated (Coleman and Baker, 1990; Bocciolone et al., 2008; Araya Reyes et al., 2023a), and well-established standards and testing procedures are in place to ensure operational safety (European Committee for Standardization (CEN), 2019). By contrast, research on road vehicles has historically prioritised aerodynamic drag reduction, with comparatively limited attention devoted to crosswind stability. The latter is addressed in ISO 12021:2010 (International Organization for Standardization, 2010), which specifies a full-scale open-loop test in which a vehicle is subjected to a constant lateral wind. However, the standard does not prescribe wind tunnel methodologies, and this omission prevents a systematic aerodynamic characterisation of road vehicles. As a result, it also hinders the alignment of the diverse experimental and numerical efforts undertaken by researchers. Although several experimental and numerical studies have examined crosswind effects on road vehicles (Cheli et al., 2006; Sterling et al.,

☆ This article is part of a Special issue entitled: 'INDAER_EACWE 2025' published in Journal of Wind Engineering & Industrial Aerodynamics.

* Corresponding author.
E-mail address: carlosesteban.araya@polimi.it (C.E. Araya Reyes).

https://doi.org/10.1016/j.jweia.2026.106578
Received 28 December 2025; Received in revised form 3 July 2026; Accepted 20 July 2026
Available online 30 July 2026

2010; Zhu et al., 2012; Han et al., 2013), the resulting datasets remain fragmented, often limited to specific vehicle categories or constrained test conditions, and are therefore of restricted general applicability.

Wind tunnel studies on heavy vehicles have demonstrated that aerodynamic loads are strongly influenced by yaw angle, turbulence, and flow separation, with significant effects on lateral force, roll moment, and vertical loads (Bocciolone et al., 2008; Cheli et al., 2011a; Araya Reyes et al., 2023b). Subsequent analyses under different infrastructure scenarios and vehicle configurations revealed that rollover risk and yaw moment behaviour vary considerably, underscoring the complexity of crosswind interactions and the need for consistent testing conditions (Cheli et al., 2011b). Experimental campaigns on bridge decks further confirmed that both vehicle type and deck configuration play a decisive role in determining aerodynamic coefficients, with lorries proving the most critical in terms of overturning stability (Dorigatti et al., 2012). More recently, systematic comparisons of flow conditions (smooth, turbulent, boundary layer) have shown that wind loads and aerodynamic moments are highly sensitive to inflow characteristics (Liu et al., 2016). Low-turbulence wind-tunnel testing provides a controlled inflow (typically of order 1% or lower freestream turbulence intensity), improving repeatability and reducing uncertainty in six-component load measurements (Cogotti, 2003; Stoll et al., 2016). This makes it suitable for isolating geometry and yaw dependent trends in aerodynamic coefficients and for constructing consistent reference datasets. Conversely, higher inflow turbulence can alter separation and wake dynamics, with corresponding changes in aerodynamic forces and moments, particularly for bluff bodies and at large yaw angles (Bocciolone et al., 2008; Passaggia et al., 2021; Bearman, 1978). Accordingly, low-turbulence inflow is widely used as a baseline condition in vehicle-aerodynamics experiments.

Additional investigations have examined bridge-related scenarios, including static vehicles on wide bridge decks (Zhang et al., 2023), moving vehicles under crosswinds (Xiang et al., 2017), and highway bridge configurations (He et al., 2020).

Although most studies have focused on high-sided vehicles, comparatively little attention has been paid to wind-tunnel investigations of crosswind effects on compact vehicles. Notable contributions include the development of the DrivAer geometry (Heft et al., 2012), which has been extensively tested in wind tunnels, primarily to generate drag-related data and to provide a publicly available benchmark for computational fluid dynamics (CFD) validation (Strangfeld et al., 2013; Wieser et al., 2014; Heft et al., 2018). While some of these studies have considered crosswind conditions, they have generally been restricted to very small yaw angles (Wieser et al., 2014, 2020), limiting their relevance for crosswind analyses involving more severe conditions.

While these studies have expanded the available database, they also reveal that most tests are carried out under specific conditions (e.g., different ground simulation strategies, scenarios, reference quantities and data-reduction procedures). As a consequence, directly comparable aerodynamic datasets across vehicle classes remain limited. This lack of consistent aerodynamic data for road vehicles represents a significant gap, particularly for the validation of CFD models and for their direct integration into vehicle dynamic simulations.

To address this gap, the present work provides a new, internally consistent dataset of mean aerodynamic force and moment coefficients for four generic road-vehicle configurations (saloon car, small lorry, double-decker coach and articulated lorry), measured in the Politecnico di Milano wind tunnel under flat-ground conditions. Tests were carried out in the low-turbulence test section to ensure repeatable and well-controlled inflow conditions.

To facilitate reuse for benchmarking and numerical validation, the complete set of aerodynamic coefficient tables is provided in Appendix. The corresponding CAD geometries of the tested models, together with the underlying experimental data supporting the reported results, are available from the authors upon request.

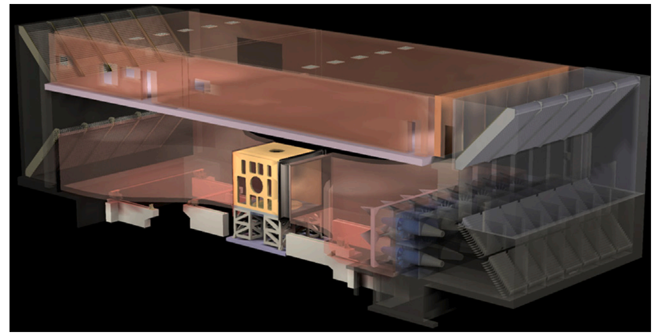

Fig. 1. Layout of the Politecnico di Milano wind tunnel.

Table 1
Principal characteristics of the Politecnico di Milano wind tunnel.

Overall dimensions	4 m wide x 3.84 m high x 6 m long
Maximum wind speed	55 m/s
Mean velocity variations in the test section	0.25%
Turbulence intensity	0.1%
Turntable	2.5 m diameter

2. Methodology

This section outlines the experimental methodology and setup adopted for the aerodynamic characterisation of generic road vehicles under crosswind conditions. The campaign was conducted at the Politecnico di Milano wind tunnel, where four vehicle models were tested at reduced geometric scale: a saloon car, a small lorry, a double-decker coach, and an articulated lorry, in order to determine their aerodynamic coefficients.

2.1. Wind tunnel facility

The experimental tests were carried out in the Wind Tunnel of Politecnico di Milano (GVPM), a vertically arranged closed-circuit facility featuring two distinct test sections located on opposite sides of the loop (Fig. 1). The upper section is designed for atmospheric boundary-layer studies, whereas the lower section provides a low-turbulence environment, where the experimental campaign described in this work was conducted. The main characteristics of this test section are summarised in Table 1.

2.2. Vehicle models

The experimental campaign considered four generic vehicle configurations representative of common road traffic and spanning both passenger and freight categories. All models were tested at reduced geometric scale (model-to-full-scale length ratio).

The tested vehicle categories were:

- **Saloon car**: a 1:4 geometric scale model of the DrivAer geometry in the closed–cooling notchback configuration. The DrivAer model is widely adopted as a benchmark for CFD validation in automotive aerodynamics (Heft et al., 2012, 2018; Wieser et al., 2014). However, published experimental investigations under crosswind conditions have typically been restricted to relatively small yaw angles (e.g. up to ±10°), with fewer datasets available at larger yaw angles that are relevant for extreme crosswind loading (Wieser et al., 2014, 2020).
- **Small lorry**: a 1:8 geometric scale model derived from the Leyland DAF, representative of a rigid-body light commercial vehicle with a high-sided, sharp-edged cab–box geometry. This vehicle class has been used in crosswind-aerodynamics studies (Sterling et al., 2010; Cheli et al., 2011a,b).

Table 2
Main dimensions of the vehicle models at model and full scale. L, W, and H denote the overall vehicle length, width, and height, respectively. Full-scale dimensions are obtained by applying the geometric scale factor (1:4 for the saloon car; 1:8 for the remaining vehicles).

	Saloon car			Small lorry			Double-decker coach			Articulated lorry		
	L	W	H	L	W	H	L	W	H	L	W	H
Model scale (mm)	1149	505	356	1023	334	442	1757	365	522.47	2057	400	500
Full scale (m)	4.596	2.020	1.424	8.184	2.672	3.536	13.816	2.920	4.179	16.456	3.200	4.000

Fig. 2. Vehicle models mounted in the Politecnico di Milano wind tunnel during the experimental campaign: (a) saloon car (DrivAer), (b) small lorry, (c) double-decker coach, (d) articulated lorry. All models are tested on the turntable under flat-ground conditions; the mounting arrangement is designed to minimise aerodynamic interference in the underbody region.

- **Double-decker coach**: a generic 1:8 geometric scale model representative of high-sided passenger transport vehicles.
- **Articulated lorry**: a generic 1:8 geometric-scale articulated freight-vehicle model, constructed according to standardised overall dimensions and comprising a tractor unit and a trailer unit. The tractor and trailer were instrumented to enable independent measurement of the aerodynamic loads acting on each unit.

For each configuration, the main dimensions are summarised in Table 2, and photographs of the models mounted in the wind tunnel are provided in Fig. 2.

2.3. *Instrumentation and fixture*

Each model was instrumented to measure aerodynamic forces and moments using a six-component internal strain-gauge balance (RUAG Aerospace Model 192-6).

The balance provides measurements of the three force components (F_x, F_y, F_z) and the three moment components (M_x, M_y, M_z).

The nominal full-scale ranges (capacities) for each channel and the corresponding manufacturer error specifications are reported in Table 3. Error values are given as per mille of full scale (‰FS), i.e. relative to the rated capacity of each channel.

Table 3
RUAG Aerospace model 192-6: Maximum values allowed for each force and moment component and corresponding errors (expressed as ‰ of full scale, FS).

Parameter	F_x (N)	F_y (N)	F_z (N)	M_x (N m)	M_y (N m)	M_z (N m)
Design load	1500	1000	5000	500	1000	600
Error std. [‰FS]	0.85	0.82	0.65	0.30	0.27	0.25
Maximum error [‰FS]	3.55	4.88	3.76	2.16	1.36	1.14

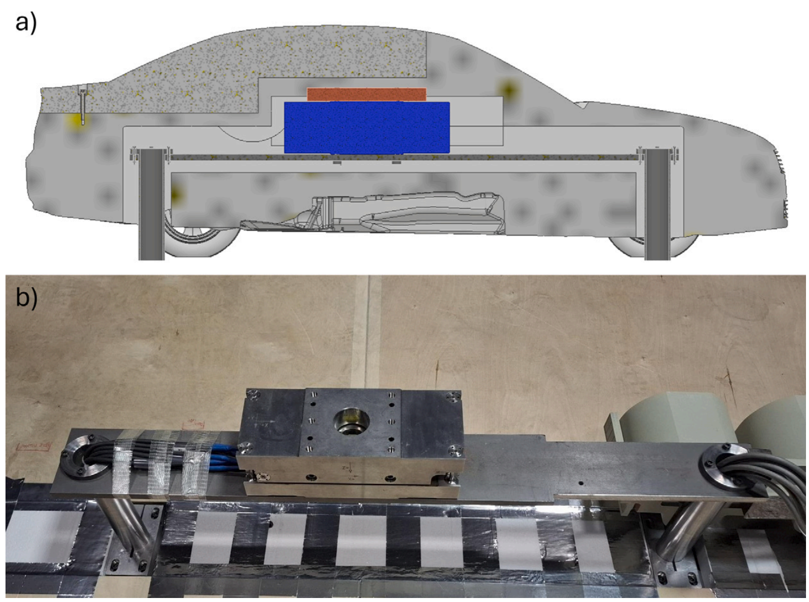

Fig. 3. Six-component balance installation used to measure aerodynamic loads. (a) CAD view of the internal arrangement, showing the RUAG Aerospace Model 192 balance mounted within the vehicle body and connected to the internal support structure. (b) Photograph of the assembled balance and support. The support is connected to the turntable through two vertical bars aligned with the wheel axles to reduce aerodynamic interference, particularly in the underbody flow region.

The balance was housed inside the model and rigidly connected to an internal support structure to ensure accurate load transmission. The support structure was anchored to the wind-tunnel turntable through two vertical bars aligned with the axles of the wheels, to minimise aerodynamic interference, particularly in the flow region of the underbody (Fig. 3).

2.4. Reference system

Aerodynamic coefficients were computed using a right-handed, vehicle-fixed Cartesian reference system following the ISO 8855 axis orientation and sign conventions (International Organization for Standardization, 2011).

The longitudinal axis x points forwards along the vehicle symmetry plane, the lateral axis y points to the left (viewed when facing forwards), and the vertical axis z points upwards.

Positive rotations follow the right-hand rule about each axis, i.e. roll about x, pitch about y, and yaw about z.

In the present work, the origin of the vehicle-fixed system used for coefficient reduction is placed at road level and centred at the midpoint of the wheelbase and track width.

Forces are therefore reported as (F_x, F_y, F_z) and moments as (M_x, M_y, M_z) about this origin, corresponding to longitudinal, lateral and vertical forces, and roll, pitch and yaw moments, respectively.

A CAD overview of the individual vehicle geometries, together with the adopted reference frames and principal dimensions, is reported in Fig. 4.

2.5. Test conditions

Aerodynamic tests were performed under a flat-ground configuration representative of open-road conditions. The vehicle models were mounted on a splitter plate, which reduces the influence of the tunnel-floor boundary layer and promotes a more uniform approach flow. The measured velocity profile above the splitter plate (Fig. 5) shows that 99% of the free-stream velocity is reached at $z = 38$ mm, which corresponds to the 99% boundary-layer thickness, δ_{99}. This is important when interpreted relative to the vehicle height H (Table 2): δ_{99}/H is 0.107 for the saloon car, 0.086 for the small lorry, 0.073 for the double-decker coach and 0.076 for the articulated lorry. Therefore, for all configurations the velocity deficit region is confined to approximately 7%–11% of the model height, so that the majority of the vehicle is exposed to an approximately uniform freestream, reducing sensitivity of the measured loads to tunnel-floor boundary-layer effects (Berndtsson et al., 1988; Farrell and Miller, 2006).

To characterise the aerodynamic response over a wide range of incident flow directions, the model was rotated on the turntable from 0° to 180° in 5° increments.

The resulting wind yaw (sideslip) angle is denoted by β (Fig. 6), with $\beta = 0°$ corresponding to head-on flow and increasing β indicating a clockwise rotation of the model about the vertical axis when viewed from above, such that $\beta = 90°$ represents a crosswind from the left and $\beta = 180°$ tail-on flow.

Test runs were performed at nominal free-stream velocities of 30 m/s and 50 m/s. No fixed velocity scale was imposed between model

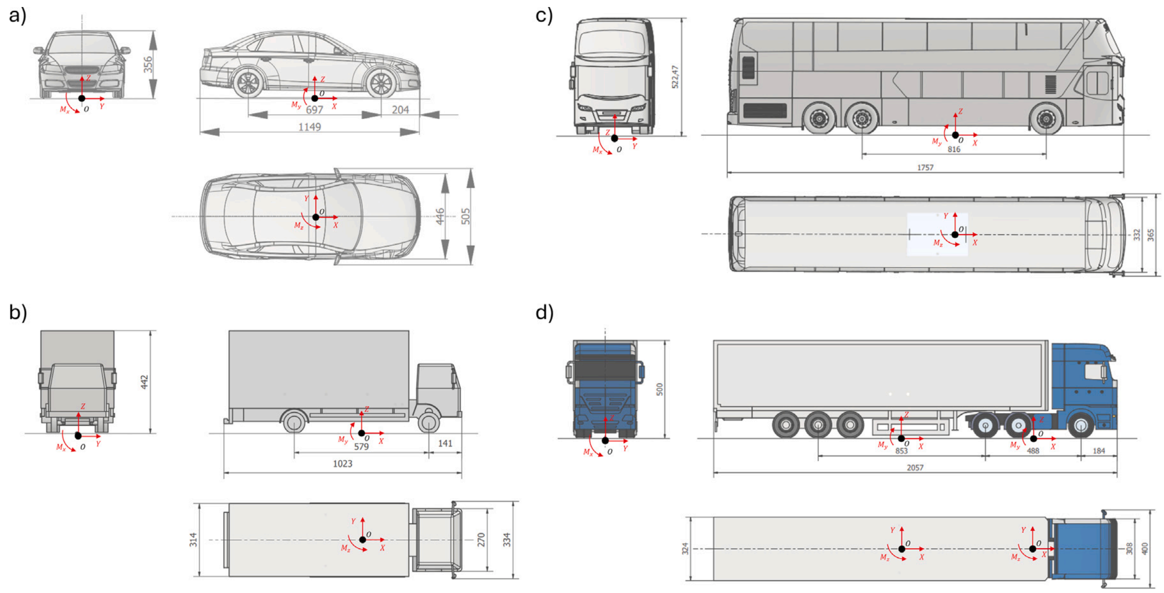

Fig. 4. CAD representations of the scaled vehicle models showing principal dimensions and the adopted reference system. The reference-frame origin is located at road level, centred at the midpoint of the wheelbase and track width; the axes follow the ISO 8855 vehicle-fixed convention. (a) saloon car (DrivAer), (b) small lorry, (c) double-decker coach, (d) articulated lorry.

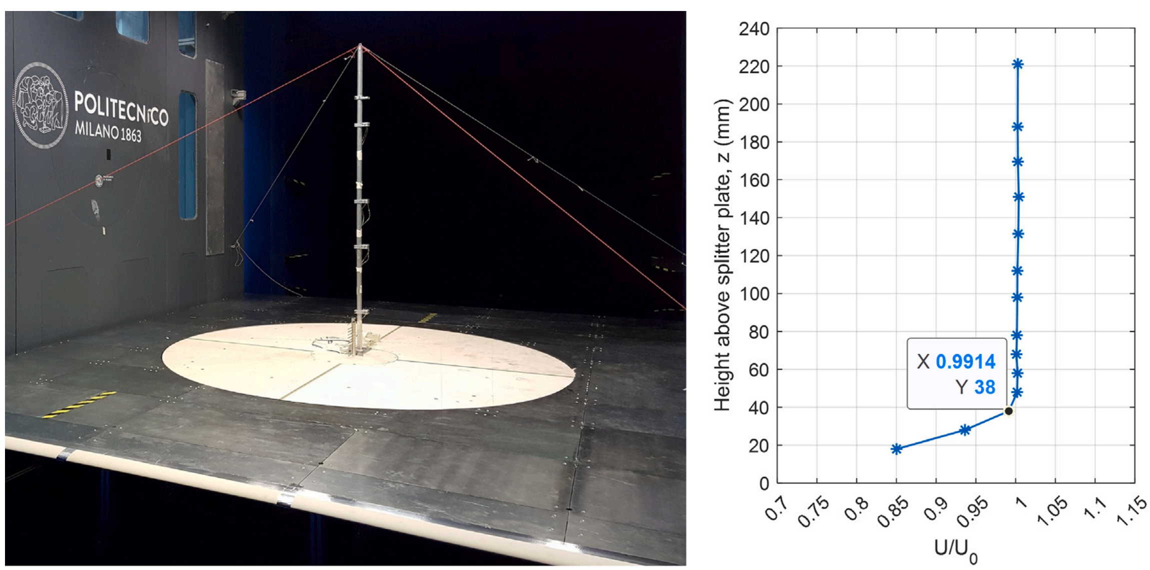

Fig. 5. Normalised streamwise velocity profile (U/U_∞) versus height above the splitter plate in the low-turbulence test section. The boundary-layer thickness based on the 99% criterion is $\delta_{99} = 38\,\mathrm{mm}$.

and full scale; instead, the tunnel speeds were selected to ensure stable measurements at sufficiently high Reynolds numbers, while the results are reported in non-dimensional coefficient form.

The Reynolds number was computed as $\mathrm{Re} = U\,L_{\mathrm{ref,scaled}}/\nu$, where $L_{\mathrm{ref,scaled}}$ is the reference length at model scale and $\nu = 1.5 \times 10^{-5}\ \mathrm{m^2/s}$ is the air kinematic viscosity under ambient laboratory conditions.

With this definition, the maximum Reynolds number (saloon car, 1:4 model at 50 m/s) is $\mathrm{Re} \approx 2.08{\times}10^6$, whereas the minimum Reynolds number (1:8 models at 30 m/s) is $\mathrm{Re} \approx 6.25 \times 10^5$.

2.6. Determination of aerodynamic coefficients

For each wind yaw (sideslip) angle β, the mean aerodynamic force and moment coefficients were computed using Eqs. (1) and (2), respectively.

$$C_{F_i}(\beta) = \frac{\overline{F_i}(\beta)}{\frac{1}{2}\,\rho\,\overline{U}^2\,A_{\mathrm{ref,scaled}}} \tag{1}$$

$$C_{M_i}(\beta) = \frac{\overline{M_i}(\beta)}{\frac{1}{2}\,\rho\,\overline{U}^2\,A_{\mathrm{ref,scaled}}\,L_{\mathrm{ref,scaled}}} \tag{2}$$

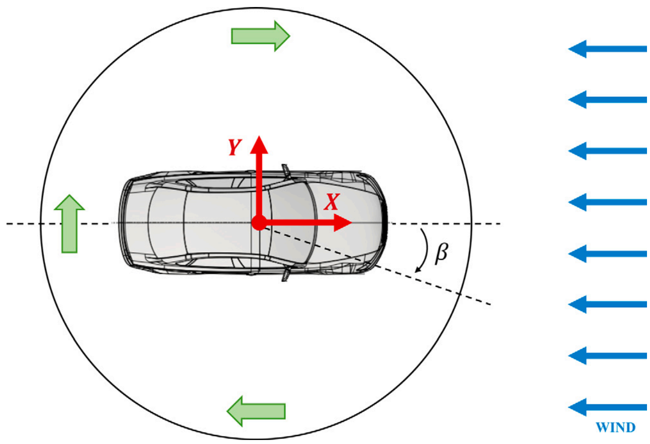

Fig. 6. Definition of the wind yaw (sideslip) angle β used in the wind-tunnel tests. The model is rotated on the turntable about the vertical axis: $\beta = 0°$ corresponds to head-on flow, and β increases with clockwise rotation when viewed from above.

Table 4
Reference dimensions for aerodynamic coefficients computation.

Reference length 2.5 m		Reference area 5 m^2	
$L_{\text{ref,scaled}}$		$A_{\text{ref,scaled}}$	
1 : 4	1 : 8	1 : 4	1 : 8
0.625 m	0.3125 m	0.3125 m^2	0.078125 m^2

where $\overline{F_i}$ denotes the time-averaged aerodynamic force along the ith axis and $\overline{M_i}$ the time-averaged aerodynamic moment about the ith axis, both referred to the origin of the adopted vehicle-fixed reference system. ρ is the air density and $\overline{U}$ is the mean freestream velocity in the test section. $A_{\text{ref,scaled}}$ and $L_{\text{ref,scaled}}$ are the reference area and reference length at model scale, obtained by applying the geometric scale factor to the chosen full-scale reference dimensions.

To enable direct comparison across vehicle classes and to facilitate identification of the most critical configurations, all coefficients are normalised using the same full-scale reference dimensions (reference length 2.5 m and reference area 5 m^2). The corresponding scaled reference quantities used in Eqs. (1)–(2) are listed in Table 4.

2.7. Validation of measurement setup against published DrivAer data

To provide an external consistency check for the present measurements, the drag coefficient of the 1:4 geometric-scale DrivAer notchback configuration at a freestream velocity of 50 m/s was compared with published wind-tunnel results by Wieser et al. (2020).

Their study reports drag-coefficient measurements for a 1:4 DrivAer notchback model at a freestream velocity of 41 m/s and for side-wind (yaw) angles from 0° up to 10° in a closed test section with splitter-plate (Wieser et al., 2020).

For a direct comparison, all drag coefficients are expressed using the same reference area adopted in the present work ($A_{\text{ref,scaled}} = 0.3125$ m^2 for the 1:4 model).

Table 5 summarises the comparison. Overall, the agreement is good: the absolute deviation is ≤ 0.003 for all yaw angles considered, corresponding to a maximum relative deviation of about 2.5%.

The small differences observed may be attributed to unavoidable facility and setup effects (e.g. flow quality, blockage correction approach, and model support interference), which are known to influence

Table 5
Validation of drag coefficient for the 1:4 DrivAer notchback configuration at $U_\infty \approx 41$ m/s. All values are reported using the same reference area adopted in this work ($A_{\text{ref,scaled}} = 0.3125$ m^2). $\Delta C_D = C_{D,\text{this work}} - C_{D,\text{ref}}$.

β [deg]	C_D (this work)	C_D (Wieser et al. 2020)	ΔC_D	$\Delta C_D/C_{D,\text{ref}}$ [%]
0	0.114	0.112	+0.002	+1.8
5	0.115	0.118	−0.003	−2.5
10	0.120	0.120	0.000	0.0

integrated aerodynamic coefficients in closed-section vehicle testing (Wieser et al., 2020; Hupertz et al., 2021). Nevertheless, the close agreement supports the consistency of the present coefficient definition and measurement methodology.

3. Results and discussions

In this section the results from the wind tunnel experimental campaign for the four vehicles analysed are presented. For each vehicle the six aerodynamic coefficients were measured.

3.1. Saloon car (DrivAer)

The results for the saloon car, based on the DrivAer geometry, are shown in Fig. 7. The figure comprises six plots showing the variation of aerodynamic coefficients over yaw angles from 0° to 180°. Force coefficients are shown on the left, while moment coefficients are presented on the right. Blue curves correspond to tests conducted at 30 m/s, and red curves represent those performed at 50 m/s.

The influence of test speed was assessed by comparing results obtained at freestream velocities of 30 m/s and 50 m/s. The associated Reynolds-number change, while moderate, spans the transcritical range commonly reported for commercial ground vehicles (width-based, with averaged values around $1.6–1.8 \times 10^6$), within which boundary-layer transition and separation behaviour can still affect aerodynamic loads, particularly for geometries whose features are not well established (smooth edges), as is the case for the saloon-car configuration (Wood, 2012).

The most pronounced differences observed in this study are in the lateral force, lift and rolling moment, particularly for wind yaw angles from 50° to 140°. This behaviour is consistent with a Reynolds-number-related delay of separation and/or modification of separated shear-layer development in yawed flow, which increases lift while reducing the lateral component of the resultant aerodynamic force. Accordingly, the combined lift–lateral force vector becomes more vertically oriented at the higher test speed, with a corresponding impact on rolling moment.

Given this speed sensitivity and to ensure a consistent reference condition, the subsequent analysis focuses on the 50 m/s results, which provide the highest Reynolds number attainable in the present facility and are therefore considered the most representative within the constraints of the experimental campaign.

The longitudinal aerodynamic force, initially negative and therefore opposing the forward motion of the vehicle, increases approximately linearly in magnitude up to a yaw angle of around 55°. Beyond this point, the magnitude gradually decreases, reaching zero near 80°, and becomes positive at larger yaw angles as the wind begins to generate a propulsive contribution when acting on the rear of the vehicle. Notably, when the flow approaches from the rear, the longitudinal force increases by approximately 25%, a behaviour reasonably attributed to the relatively square geometry of the rear end.

Abrupt variations are observed in the range $\beta \approx 50°–60°$ and $\beta \approx 130°–150°$, most clearly in C_{F_y}, C_{F_z} and C_{M_x}. These features suggest a change in the dominant flow regime as the incident direction progresses from more streamlined (slender-body-like) loading to a configuration

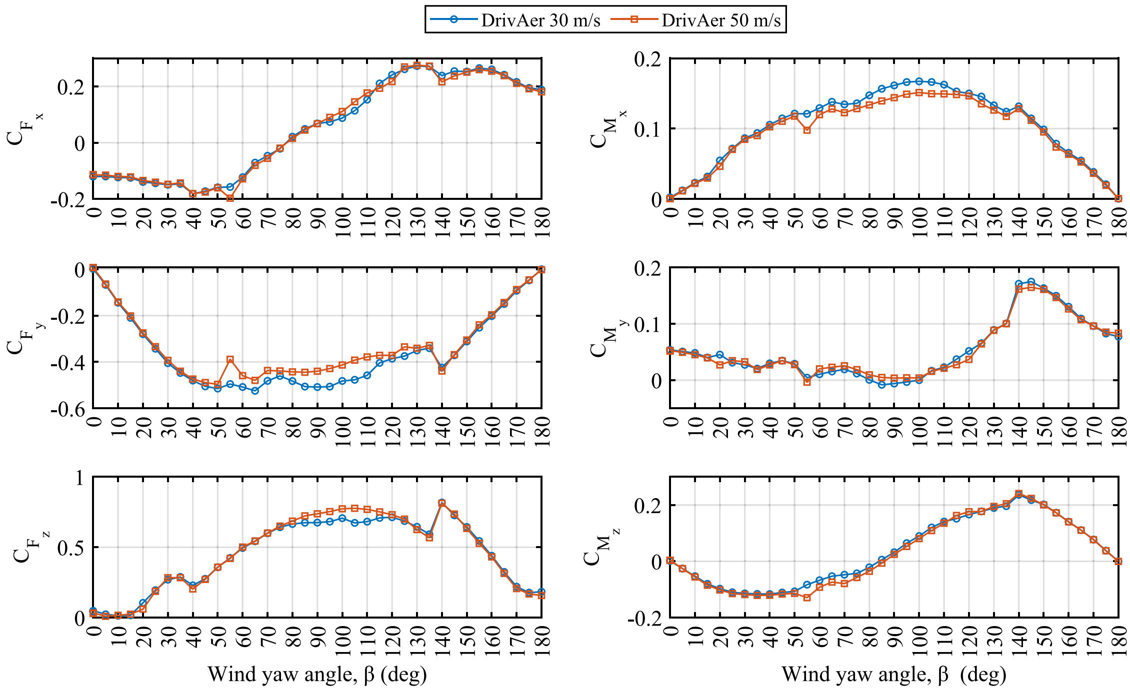

Fig. 7. Aerodynamic coefficients for Saloon Car model.

in which the vehicle presents a broader projected area to the flow and separation/wake effects become more influential.

While the present study does not include flow visualisation or surface-pressure tecnics, these changes are consistent with published side-wind investigations of DrivAer-type geometries, which show that yawed inflow can substantially modify the formation and strength of vortical structures (including those associated with the A-pillar and C-pillar) and lead to a reorganisation of the near wake and rear pressure recovery (Wieser et al., 2014, 2020). In particular, Wieser et al. report that side-wind angles can produce a marked change in wake topology, with the yawed-flow state dominated by different longitudinal vortices compared to the nominally symmetric baseline (Wieser et al., 2020).

Accordingly, the observed coefficient inflections at $\beta \approx 50°–60°$ and $\beta \approx 130°–150°$ are interpreted here as indicative of a transition between distinct wake/topology states.

With regard to the pitch moment, it is noteworthy that it remains mostly positive regardless of wind direction. A positive pitch moment under headwind conditions is not straightforward to interpret. This behaviour, however, is consistent with findings reported in previous research (Heft et al., 2012; Hupertz et al., 2021), who have shown that, for the closed-cooling/notchback configuration of the DrivAer model, the lift distribution is predominantly rear-biased: the rear section generates most of the lift, whereas the front contributes mainly to downforce. Such a distribution of aerodynamic forces naturally leads to the predominantly positive pitch moment observed in the measurements.

Finally, it is possible to comment on the yaw moment coefficient. In this case, an S-shaped trend is observed, with negative yaw moment coefficients recorded for wind yaw angles below 85°. This indicates that the wind induces a moment which tends to rotate the vehicle in the direction of the flow, that is, causing the front of the vehicle to turn towards the leeward side.

3.1.1. Small lorry

Fig. 8 presents the aerodynamic results for the small lorry. As with the saloon car, six plots are provided, covering yaw angles from 0° to 180°. Force coefficients are shown on the left, while moment coefficients are displayed on the right. Blue curves correspond to measurements taken at 30 m/s, and red curves represent those obtained at 50 m/s.

In contrast to the behaviour observed with the DrivAer model, the small lorry exhibits minimal differences between the results obtained at wind speeds of 30 m/s and 50 m/s, as shown in Fig. 8. This suggests that, within the Reynolds-number range investigated in this campaign, Reynolds-number effects are negligible for the small lorry configuration. Although there is a slight variation with speed in the magnitude of the lift coefficient, the conclusions drawn from the data remain unaffected.

The longitudinal aerodynamic coefficient C_{F_x} is negative at a yaw angle of 0° and remains so up to approximately 75°. Within this range, the minimum value, corresponding to the largest magnitude under headwind conditions, is achieved at a yaw angle close to 20°. Beyond 75°, C_{F_x} becomes positive, indicating a reversal in the direction of the longitudinal force. Around 105°, the coefficient returns to negative values, before increasing again and remaining positive at higher yaw angles.

In this case, the lateral-force coefficient varies smoothly with yaw angle, with no marked discontinuities. The small lorry, characterised by sharp edges and a rectilinear cab–box geometry, exhibits a response consistent with bluff-body behaviour across the full yaw range. Accordingly, no distinct regime change is evident in the lateral-force trend. The lateral force remains negative and shows an approximately symmetric dependence on yaw angle, indicating that the load response is dominated by the box-body geometry.

The vertical aerodynamic coefficient is positive throughout the entire yaw angle range, indicating that the small lorry consistently generates lift. From 0° to approximately 40°, the lift increases with

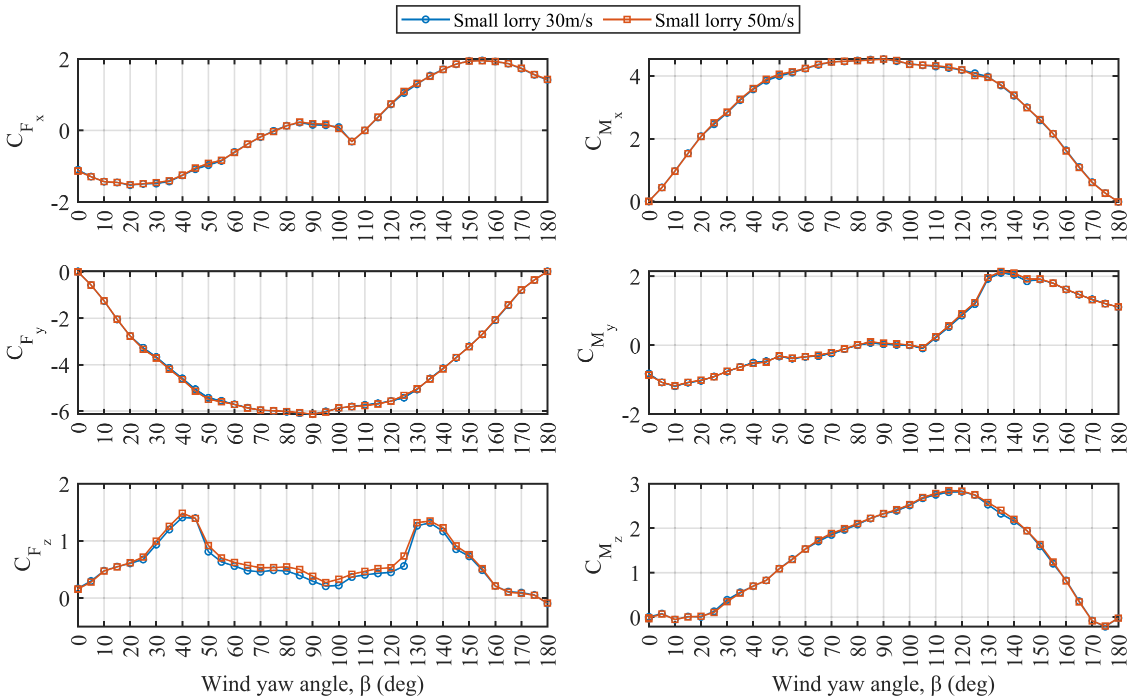

Fig. 8. Aerodynamic coefficients for Small Lorry model.

a nearly linear trend. Beyond this point, it begins to decrease in a non linear manner, reaching a minimum around 95°. The coefficient then increases again to 135°, before undergoing a final decline and approaching zero near 180°.

The roll moment coefficient exhibits a trend closely aligned with that of C_{F_y}, indicating that the rolling moment is governed predominantly by the distribution of lateral force rather than by the vertical force. Although the roll moment depends on both lateral and vertical resultant forces, the similarity in trends suggests that the vertical distance between the centre of pressure and the roll axis remains approximately constant across yaw angles, and that the resultant lift force lies close to the longitudinal vertical plane. Consequently, the contribution of the vertical force to the total rolling moment is negligible, confirming the dominant role of lateral force distribution.

In the case of the small lorry, the pitch moment coefficient, and thus the pitch moment, is governed by the combined influence of the longitudinal and vertical aerodynamic forces, in contrast to the car, where the vertical force plays the dominant role. At small yaw angles, the coefficient becomes negative in line with C_{F_x}, reflecting the dominance of the longitudinal force. As the vertical force increases, its contribution produces a more linear variation of the coefficient with yaw angle than that associated with the longitudinal force alone. At intermediate yaw angles between 60° and 120°, both the vertical and longitudinal forces are relatively small, and the pitch moment therefore approaches zero. Beyond 120°, the pitch moment is again governed by a combination of longitudinal and vertical forces; however, the longitudinal force acts in the opposite sense, causing the coefficient to become positive. In the final part of the range, as the lift force decreases, the pitch moment is once more dominated by the longitudinal force.

The yaw moment remains close to zero at small yaw angles, below approximately 25°. Beyond this range, a positive yaw moment coefficient is observed. The initial behaviour results from the combined influence of the longitudinal force, which tends to produce a negative yawing effect, and the position of the resultant lateral force, whose application point lies behind the mid-wheelbase reference point used for moment reduction. In contrast to the behaviour observed for the sedan car, the yaw moment of the small lorry tends to rotate the vehicle against the incoming flow for yaw angles greater than 20°.

If we analyse how these differences affect vehicle handling, the yawing response becomes particularly significant. For the sedan car, the negative yaw moment observed at yaw angles below 85° tends to rotate the vehicle in the direction of the flow, turning the front towards the leeward side. Although destabilising, this effect can be compensated relatively smoothly and intuitively by corrective steering inputs, since the induced rotation aligns with the natural drift of the vehicle under crosswind. In contrast, the small lorry exhibits a positive yaw moment beyond 20°, which tends to rotate the vehicle against the incoming flow. This behaviour requires more active counter-steering from the driver, as the corrective action must oppose the intuitive steering response.

3.1.2. Double-decker coach and articulated lorry

In Fig. 9, the wind tunnel results for the aerodynamic coefficients of the double-decker coach (red line), the articulated lorry tractor (yellow line) and trailer (purple line) are presented alongside those of the small lorry (blue line), thereby providing a comparative overview of the three high-sided vehicles. As with the previous presented results, six plots are provided, covering yaw angles from 0° to 180°. The left-hand panels display the force coefficients, while the right-hand panels show the moment coefficients. The data derive from wind tunnel tests on 1:8 scale models, performed at 30 m/s for the double-decker coach and articulated lorry, and at 50 m/s for the small lorry.

The longitudinal-force coefficient C_{F_x} of the double-decker coach shows a broadly similar yaw dependence to that of the small lorry, but with a more irregular evolution, particularly around $\beta \approx 50°$, 85° and 125°. A plausible explanation is that the coach geometry, with comparatively less pronounced edges and smoother curvature, promotes

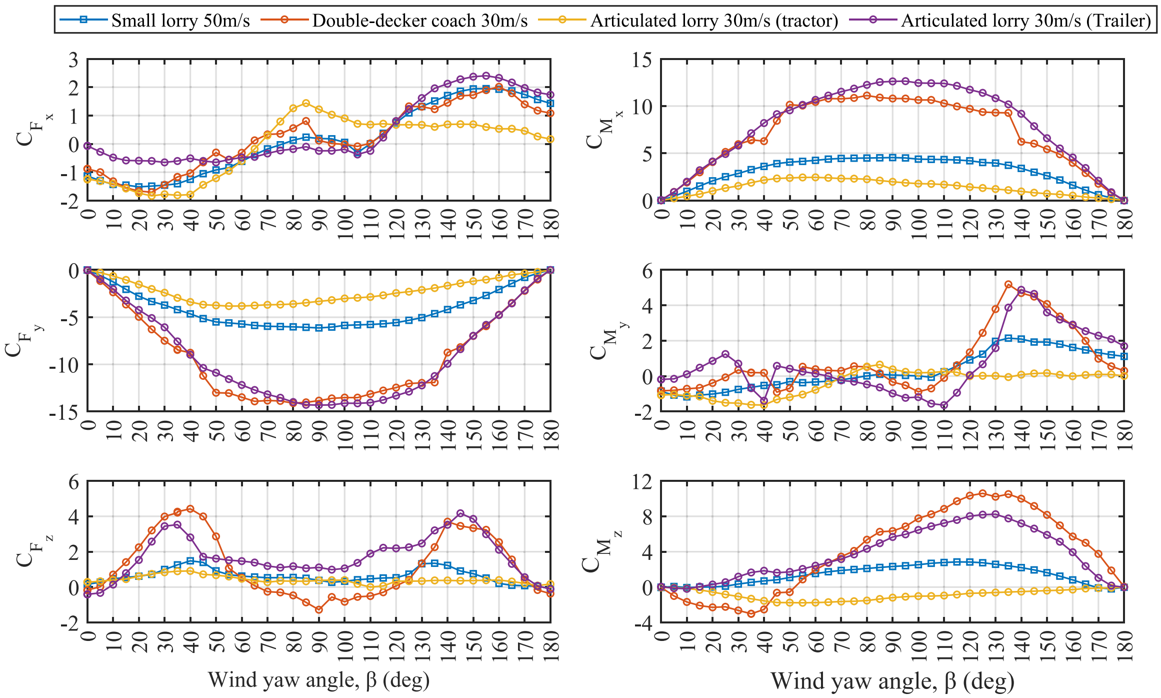

Fig. 9. Aerodynamic coefficients for the three high sided vehicles: Small lorry (blue), Double-decker coach (red), Articulated lorry tractor (yellow) and trailer (purple).

separation and reattachment in different regions as the incident direction changes, leading to localised changes in the pressure distribution and therefore in the integrated C_{F_x}. Consistently, the same yaw-angle intervals are also reflected in the lateral-force and rolling-moment coefficients, indicating coupled variations of the overall aerodynamic loading.

For the articulated lorry, the trailer exhibits markedly smaller C_{F_x} magnitudes at low yaw angles, consistent with partial shielding by the upstream tractor unit in the coupled configuration. In contrast, the tractor response at low yaw angles is comparable to that of the small lorry; however, the sign change of C_{F_x} occurs at a substantially lower yaw angle (around $\beta \approx 65°$), and the peak forward-force is observed near $\beta \approx 85°$. These differences are consistent with tractor–trailer aerodynamic interaction, which modifies the local flow field around the tractor and alters the longitudinal component of the resultant aerodynamic force.

For the double-decker coach the side force increases almost linearly with the yaw angle up to 35°−−40°, where a sudden jump occurs, probably due to changes in the vortex structures typically found along the vehicle sides at small side wind angles, which vanish at higher angles. From 50° onwards, the coefficient remains approximately constant up to 90°, then decreases gradually until 135°, where another jump is observed. Beyond 140°, C_{F_y} decreases linearly. The trailer unit of the articulated lorry, being similar in dimensions to the double-decker coach, exhibits comparable values, with an almost identical peak. In this case, the trend is much smoother, resembling that observed for the small lorry. This behaviour is consistent with the sharp-edged trailer geometry, which promotes separation in a comparatively repeatable manner and therefore leads to smoother C_{F_x} variations with yaw angle.

The vertical force coefficient shows a trend similar to that of the small lorry, but at intermediate yaw angles it reaches negative values, indicating that the coach generates downforce in the range 70°−−120°. For yaw angles below 70°, the lift force remains positive, with the peak occurring around 40°.

As observed for the small lorry, the double-decker coach rolling-moment coefficient closely follows the lateral-force coefficient, indicating that side loading is the dominant contributor to roll response and, therefore, to crosswind stability. Turning to the pitching moment, its magnitude remains comparatively small over most of the yaw range. It changes sign for yaw angles below approximately 100°–110°, then increases rapidly up to about 135°, before decreasing again towards zero as $\beta \to 180°$.

Finally, the yawing-moment coefficient is negative at small yaw angles, where the longitudinal force contribution is dominant. Beyond about 40°, C_{M_z} increases and becomes positive at larger yaw angles as the side force becomes the dominant component. This trend suggests a rearward shift of the effective line of action of the lateral load relative to the reduction point.

4. Conclusions

In this paper, wind-tunnel experiments were performed on four generic road-vehicle configurations representative of passenger and commercial transport: a saloon car (DrivAer notchback), a small lorry, a double-decker coach, and an articulated lorry (tractor–trailer). Tests were conducted in the low-turbulence test section of the Politecnico di Milano wind tunnel under a flat-ground configuration, and aerodynamic force and moment coefficients were obtained over a full wind-yaw range ($0° \leq \beta \leq 180°$) using consistent coefficient definitions and reference quantities across all vehicles.

A validation check was performed to experimental setup by comparing the present drag coefficients for the saloon-car configuration against published data ($0° \leq \beta \leq 10°$) using the same reference area definition. The agreement is good, with deviations within ±0.003 in C_D, supporting the robustness of the adopted coefficient definitions and experimental methodology (Wieser et al., 2020).

Across all configurations, the results demonstrate a strong and systematic dependence of aerodynamic loads on vehicle geometry and wind yaw angle, with pronounced differences between the low-profile saloon car and the high-sided commercial vehicles. High-sided vehicles experience substantially larger lateral-force and rolling-moment coefficients: peak values for the double-decker coach and for the trailer unit of the articulated lorry are up to approximately thirty times higher than those of the saloon car.

For the saloon car, a clear sensitivity to test speed was observed in the lateral force, lift, and rolling moment, most notably in yawed inflow. This behaviour is consistent with Reynolds-number effects in the transcritical range reported for ground vehicles, where boundary-layer transition and separation can influence aerodynamic loads (Wood, 2012). For the more bluff, sharp-edged commercial configurations, the measured coefficients showed comparatively small variation with test speed within the accessible Reynolds-number range.

The coefficient trends across the investigated wind-yaw range reveal distinct non-linear features. Abrupt changes in the side-force and rolling-moment coefficients occur at specific yaw angles for the smoother geometries. In the absence of flow-visualisation or surface-pressure diagnostics in the present campaign, these features are interpreted as indicators of changes in the dominant separation and wake organisation, consistent with previously reported DrivAer side-wind investigations that demonstrate yaw-induced modifications of vortical structures and wake topology (Wieser et al., 2014, 2020).

Overall, the use of uniform testing conditions and data-reduction procedures across all configurations has produced a coherent and directly comparable dataset of aerodynamic coefficients over a wide range of incident flow directions. This dataset is well suited for comparative assessments across vehicle classes, for use as input to vehicle-dynamics simulations, and as reference data for CFD validation in crosswind conditions. Future work may naturally extend the present results by complementing force and moment measurements with flow-field diagnostics (e.g., PIV and/or surface-pressure measurements) to further resolve the mechanisms underlying the observed non-linear features.

To facilitate reuse of the results for benchmarking, model intercomparisons and CFD validation, the full aerodynamic coefficient dataset is reported in Appendix; the CAD geometries associated with the models, together with the underlying experimental data supporting the reported results, are available from the authors upon request.

CRediT authorship contribution statement

Carlos Esteban Araya Reyes: Writing – review & editing, Writing – original draft, Methodology, Investigation, Formal analysis, Data curation, Conceptualization. **Irene Lechiguero Pardo:** Writing – original draft, Data curation. **Stefano Negri:** Methodology, Investigation, Data curation. **Gisella Tomasini:** Writing – review & editing, Supervision, Resources, Project administration, Formal analysis, Conceptualization.

Declaration of competing interest

The authors declare that they have no known competing financial interests or personal relationships that could have appeared to influence the work reported in this paper.

Acknowledgement

The project CROSS-STORM has been funded by EU, NextGenerationEU, M4C2 I1.1, Project PRIN 2022 PNRR “CROSS-STORM”, Prot. 202284ZER9, CUP D53D23003170006.

Appendix. Aerodynamic coefficients

A.1. Saloon car (DrivAer notchback)

See Table A.6.

A.2. Small lorry

See Table A.7.

A.3. Double-decker coach

See Table A.8.

A.4. Articulated lorry tractor unit

See Table A.9.

A.5. Articulated lorry trailer unit

See Table A.10.

Data availability

Data will be made available on request.

Table A.6
Mean aerodynamic coefficients for the saloon car (DrivAer notchback), $U_\infty = 50\,\mathrm{m/s}$.

β [°]	C_{F_x}	C_{F_y}	C_{F_z}	C_{M_x}	C_{M_y}	C_{M_z}
0	−0.114	0.007	0.033	0.001	0.052	0.004
5	−0.115	−0.064	0.010	0.012	0.049	−0.026
10	−0.120	−0.141	0.017	0.022	0.045	−0.056
15	−0.121	−0.201	0.025	0.030	0.040	−0.085
20	−0.134	−0.275	0.061	0.046	0.027	−0.102
25	−0.140	−0.334	0.187	0.070	0.035	−0.115
30	−0.148	−0.393	0.284	0.085	0.033	−0.118
35	−0.143	−0.440	0.284	0.090	0.019	−0.121
40	−0.181	−0.474	0.204	0.103	0.027	−0.121
45	−0.175	−0.489	0.272	0.110	0.035	−0.116
50	−0.160	−0.496	0.359	0.118	0.028	−0.114
55	−0.197	−0.388	0.420	0.098	−0.004	−0.129
60	−0.129	−0.459	0.501	0.120	0.020	−0.092
65	−0.081	−0.479	0.545	0.128	0.023	−0.074
70	−0.055	−0.437	0.601	0.123	0.026	−0.079
75	−0.019	−0.439	0.650	0.128	0.019	−0.057
80	0.015	−0.443	0.686	0.134	0.009	−0.035
85	0.045	−0.444	0.723	0.139	0.005	−0.007
90	0.068	−0.440	0.737	0.144	0.004	0.025
95	0.090	−0.428	0.753	0.149	0.004	0.053
100	0.111	−0.413	0.773	0.151	0.004	0.081
105	0.145	−0.392	0.777	0.150	0.016	0.109
110	0.177	−0.378	0.769	0.149	0.021	0.135
115	0.193	−0.371	0.751	0.148	0.027	0.163
120	0.217	−0.372	0.731	0.147	0.037	0.176
125	0.269	−0.335	0.700	0.135	0.064	0.177
130	0.275	−0.341	0.625	0.126	0.088	0.195
135	0.272	−0.329	0.568	0.117	0.100	0.205
140	0.216	−0.439	0.813	0.128	0.162	0.241
145	0.237	−0.368	0.736	0.112	0.165	0.224
150	0.250	−0.305	0.634	0.095	0.161	0.200
155	0.259	−0.240	0.528	0.074	0.147	0.172
160	0.254	−0.196	0.431	0.064	0.126	0.140
165	0.238	−0.144	0.314	0.053	0.107	0.110
170	0.211	−0.088	0.207	0.037	0.096	0.077
175	0.191	−0.046	0.168	0.019	0.085	0.038
180	0.180	−0.002	0.157	0.001	0.083	−0.000

Table A.7
Mean aerodynamic coefficients for the small lorry, $U_\infty = 50\,\mathrm{m/s}$.

β [°]	C_{F_x}	C_{F_y}	C_{F_z}	C_{M_x}	C_{M_y}	C_{M_z}
0	−1.139	0.003	0.159	0.002	−0.863	−0.015
5	−1.296	−0.565	0.279	0.439	−1.074	0.071
10	−1.433	−1.244	0.473	0.962	−1.173	−0.051
15	−1.455	−2.038	0.546	1.523	−1.073	0.004
20	−1.518	−2.766	0.618	2.068	−1.011	0.021
25	−1.490	−3.333	0.718	2.508	−0.914	0.105
30	−1.459	−3.711	0.997	2.846	−0.751	0.349
35	−1.408	−4.193	1.257	3.259	−0.634	0.540
40	−1.252	−4.639	1.485	3.601	−0.526	0.700
45	−1.053	−5.141	1.394	3.895	−0.487	0.828
50	−0.921	−5.498	0.919	4.055	−0.307	1.088
55	−0.836	−5.597	0.702	4.135	−0.371	1.296
60	−0.618	−5.717	0.624	4.243	−0.330	1.534
65	−0.383	−5.868	0.573	4.372	−0.286	1.736
70	−0.177	−5.956	0.531	4.445	−0.209	1.886
75	−0.033	−5.984	0.533	4.470	−0.103	1.991
80	0.129	−6.018	0.545	4.486	0.013	2.107
85	0.236	−6.068	0.501	4.511	0.101	2.225
90	0.190	−6.131	0.383	4.536	0.064	2.331
95	0.178	−6.043	0.271	4.494	0.039	2.416
100	0.053	−5.858	0.330	4.371	0.013	2.533
105	−0.309	−5.811	0.417	4.347	−0.065	2.692
110	0.003	−5.767	0.468	4.327	0.248	2.784
115	0.374	−5.694	0.516	4.282	0.565	2.845
120	0.744	−5.571	0.530	4.197	0.912	2.835
125	1.093	−5.322	0.736	4.013	1.240	2.753
130	1.319	−5.043	1.319	3.955	1.966	2.578
135	1.515	−4.616	1.349	3.718	2.144	2.405
140	1.707	−4.182	1.230	3.392	2.094	2.202
145	1.859	−3.685	0.913	2.985	1.926	1.943
150	1.941	−3.226	0.759	2.611	1.922	1.634
155	1.950	−2.687	0.515	2.158	1.804	1.241
160	1.930	−2.058	0.212	1.605	1.622	0.815
165	1.871	−1.416	0.103	1.078	1.477	0.343
170	1.742	−0.771	0.083	0.598	1.320	−0.084
175	1.565	−0.345	0.049	0.260	1.205	−0.199
180	1.429	0.021	−0.087	−0.017	1.115	−0.021

Table A.8
Mean aerodynamic coefficients for the double-decker, $U_\infty = 30\,\mathrm{m/s}$.

β [°]	C_{F_x}	C_{F_y}	C_{F_z}	C_{M_x}	C_{M_y}	C_{M_z}
0	−0.883	−0.030	−0.165	0.023	−0.830	−0.032
5	−1.000	−1.152	0.021	0.894	−0.801	−0.997
10	−1.321	−2.353	0.708	1.901	−0.717	−1.675
15	−1.550	−3.644	1.410	2.975	−0.663	−2.087
20	−1.667	−4.955	2.248	4.057	−0.388	−2.285
25	−1.707	−6.285	3.203	5.136	−0.073	−2.225
30	−1.444	−7.491	3.986	5.960	0.349	−2.636
35	−1.170	−8.466	4.258	6.422	0.202	−3.016
40	−1.036	−8.765	4.423	6.276	0.186	−2.522
45	−0.653	−11.211	3.992	8.440	−0.906	−0.634
50	−0.306	−13.006	2.864	10.136	−0.687	−0.565
55	−0.561	−13.046	1.066	10.049	0.531	0.871
60	−0.315	−13.486	0.533	10.435	0.390	1.963
65	0.124	−13.920	0.085	10.796	0.321	2.738
70	0.334	−13.834	−0.257	10.767	0.297	3.436
75	0.355	−13.875	−0.299	10.862	0.556	4.089
80	0.553	−14.110	−0.467	11.114	0.519	5.357
85	0.808	−14.026	−0.862	10.899	0.161	6.251
90	0.119	−13.844	−1.277	10.799	−0.333	6.332
95	0.014	−13.606	−0.558	10.794	−0.521	6.853
100	−0.019	−13.520	−0.826	10.644	−0.886	7.765
105	−0.089	−13.526	−0.549	10.647	−0.695	8.231
110	0.019	−13.144	−0.505	10.290	−0.101	8.835
115	0.338	−12.773	−0.292	9.961	0.615	9.707
120	0.795	−12.461	0.075	9.703	1.343	10.333
125	1.325	−12.030	0.410	9.366	2.442	10.592
130	1.311	−11.961	1.341	9.301	3.787	10.209
135	1.225	−11.914	2.259	9.273	5.185	10.507
140	1.450	−8.741	3.696	6.218	4.693	9.993
145	1.696	−8.175	3.455	6.017	4.491	9.160
150	1.722	−6.986	3.335	5.422	4.073	8.163
155	1.897	−5.952	3.237	4.887	3.367	6.973
160	2.015	−4.736	2.539	3.976	2.869	5.721
165	1.788	−3.480	1.560	2.896	1.991	5.006
170	1.395	−2.198	0.427	1.759	0.984	3.757
175	1.176	−0.999	−0.162	0.784	0.554	1.879
180	1.082	0.038	−0.371	−0.017	0.301	0.046

Table A.9
Mean aerodynamic coefficients for the articulated lorry tractor unit, $U_\infty = 30\,\mathrm{m/s}$.

β [°]	C_{F_x}	C_{F_y}	C_{F_z}	C_{M_x}	C_{M_y}	C_{M_z}
0	−1.239	−0.011	0.277	0.004	−1.067	−0.012
5	−1.317	−0.273	0.329	0.215	−1.042	−0.064
10	−1.409	−0.619	0.402	0.435	−1.107	−0.156
15	−1.575	−1.040	0.454	0.666	−1.150	−0.318
20	−1.738	−1.522	0.614	0.992	−1.393	−0.554
25	−1.837	−2.005	0.746	1.306	−1.505	−0.828
30	−1.779	−2.396	0.837	1.531	−1.528	−1.057
35	−1.815	−2.943	0.897	1.871	−1.620	−1.316
40	−1.791	−3.382	0.914	2.151	−1.634	−1.550
45	−1.448	−3.664	0.720	2.321	−1.318	−1.740
50	−1.213	−3.742	0.674	2.375	−1.188	−1.755
55	−0.954	−3.816	0.598	2.431	−1.040	−1.771
60	−0.605	−3.808	0.472	2.440	−0.777	−1.750
65	−0.179	−3.751	0.366	2.387	−0.459	−1.702
70	0.297	−3.680	0.280	2.314	−0.078	−1.626
75	0.788	−3.656	0.349	2.301	0.227	−1.596
80	1.258	−3.594	0.336	2.239	0.539	−1.518
85	1.439	−3.461	0.330	2.099	0.650	−1.342
90	1.218	−3.310	0.378	1.970	0.380	−1.188
95	1.030	−3.185	0.393	1.860	0.242	−1.081
100	0.900	−3.005	0.395	1.772	0.186	−1.017
105	0.708	−2.932	0.182	1.744	0.202	−1.010
110	0.679	−2.849	0.003	1.675	0.257	−0.951
115	0.710	−2.672	0.066	1.568	0.215	−0.841
120	0.673	−2.430	0.332	1.410	−0.004	−0.700
125	0.676	−2.288	0.338	1.311	0.020	−0.663
130	0.670	−2.105	0.342	1.201	0.016	−0.609
135	0.600	−1.901	0.378	1.086	−0.053	−0.555
140	0.688	−1.650	0.378	0.946	0.079	−0.505
145	0.695	−1.398	0.361	0.812	0.150	−0.454
150	0.690	−1.172	0.369	0.703	0.174	−0.394
155	0.595	−1.008	0.389	0.630	0.075	−0.350
160	0.530	−0.786	0.398	0.503	−0.008	−0.278
165	0.534	−0.501	0.315	0.352	0.064	−0.159
170	0.458	−0.346	0.212	0.239	0.097	−0.119
175	0.262	−0.192	0.087	0.125	0.095	−0.084
180	0.168	−0.010	0.174	0.015	0.011	−0.005

Table A.10
Mean aerodynamic coefficients for the articulated lorry trailer unit, $U_\infty = 30\,\mathrm{m/s}$.

β [°]	C_{F_x}	C_{F_y}	C_{F_z}	C_{M_x}	C_{M_y}	C_{M_z}
0	−0.069	−0.017	−0.409	0.016	−0.186	0.035
5	−0.283	−0.962	−0.325	0.879	−0.153	−0.119
10	−0.483	−2.022	0.143	1.979	0.105	−0.193
15	−0.585	−3.225	0.787	3.192	0.477	0.056
20	−0.595	−4.224	1.533	4.119	0.858	0.294
25	−0.604	−5.086	2.572	4.916	1.247	0.554
30	−0.653	−6.066	3.443	5.807	0.704	1.179
35	−0.606	−7.565	3.529	7.118	−0.682	1.654
40	−0.511	−8.971	2.807	8.198	−1.390	1.852
45	−0.603	−10.377	1.716	9.139	0.580	1.630
50	−0.654	−10.885	1.612	9.550	0.416	1.719
55	−0.557	−11.558	1.522	10.126	0.253	2.050
60	−0.478	−12.184	1.469	10.655	0.143	2.420
65	−0.460	−12.719	1.388	11.110	−0.001	2.784
70	−0.338	−13.178	1.192	11.520	−0.242	3.173

(continued on next page)

Table A.10 (*continued*).

β [°]	C_{F_x}	C_{F_y}	C_{F_z}	C_{M_x}	C_{M_y}	C_{M_z}
75	−0.233	−13.540	1.101	11.847	−0.313	3.694
80	−0.183	−13.993	1.179	12.244	−0.469	4.331
85	−0.102	−14.284	1.064	12.542	−0.640	4.964
90	−0.246	−14.323	1.111	12.616	−0.978	5.660
95	−0.243	−14.294	0.986	12.642	−1.226	5.960
100	−0.195	−14.112	1.057	12.444	−1.184	6.457
105	−0.375	−14.132	1.367	12.421	−1.554	6.871
110	−0.246	−14.064	1.891	12.402	−1.640	7.230
115	0.223	−13.771	2.222	12.143	−0.938	7.591
120	0.806	−13.315	2.191	11.733	0.055	8.020
125	1.233	−12.888	2.249	11.399	0.667	8.185
130	1.616	−12.231	2.467	10.829	1.582	8.235
135	1.961	−11.240	3.204	10.181	3.870	7.761
140	2.122	−9.934	3.521	9.177	4.874	7.198
145	2.279	−8.383	4.171	7.864	4.644	6.607
150	2.372	−6.965	3.853	6.591	3.599	5.896
155	2.406	−5.807	2.989	5.504	3.195	5.128
160	2.329	−4.764	2.111	4.546	2.909	3.946
165	2.166	−3.531	1.315	3.428	2.540	2.372
170	1.972	−2.134	0.559	2.078	2.285	1.048
175	1.814	−0.898	0.072	0.861	2.087	0.170
180	1.733	0.016	−0.112	−0.015	1.691	−0.013

References

Araya Reyes, C.E., Brambilla, E., Tomasini, G., 2023a. Evaluation of the aerodynamic effect of a smooth rounded roof on crosswind stability of a train by wind tunnel tests. Appl. Sci. 13 (1), 232. http://dx.doi.org/10.3390/app13010232.

Araya Reyes, C.E., Rocchi, D., Tomasini, G., Iraeta Sánchez, M., Artano, M., 2023b. Effects of different aerodynamic configurations on crosswind stability of a conventional train. J. Wind Eng. Ind. Aerodyn. 242, 105588. http://dx.doi.org/10.1016/j.jweia.2023.105588.

Baker, C.J., Reynolds, S., 1991. Wind induced accidents of road vehicles. Accid. Anal. Prev. 24 (6), 559–575. http://dx.doi.org/10.1016/0001-4575(92)90009-8.

Bearman, P.W., 1978. Some effects of free-stream turbulence and the presence of the ground on the flow around bluff bodies. In: Sovran, G., Morel, T., Mason, W.T. (Eds.), Aerodynamic Drag Mechanisms of Bluff Bodies and Road Vehicles. Springer, Boston, MA, pp. 95–127. http://dx.doi.org/10.1007/978-1-4684-8434-2_4.

Becker, N., Rust, H.W., Ulbrich, U., 2022. Weather impacts on various types of road crashes: a quantitative analysis using generalized additive models. Eur. Transp. Res. Rev. 14 (1), 37. http://dx.doi.org/10.1186/s12544-022-00561-2.

Berndtsson, A., Eckert, W.T., Mercker, E., 1988. The effect of groundplane boundary layer control on automotive testing in a wind tunnel. In: SAE International Congress and Exposition. SAE International, http://dx.doi.org/10.4271/880248.

Bocciolone, M., Cheli, F., Corradi, R., Muggiasca, S., Tomasini, G., 2008. Crosswind action on rail vehicles: Wind tunnel experimental analyses. J. Wind Eng. Ind. Aerodyn. 96 (5), 584–610. http://dx.doi.org/10.1016/j.jweia.2008.02.030.

Cheli, F., Belforte, P., Melzi, S., Sabbioni, E., Tomasini, G., 2006. Numerical–experimental approach for evaluating cross-wind aerodynamic effects on heavy vehicles. Veh. Syst. Dyn. 44 (sup1), 791–804. http://dx.doi.org/10.1080/00423110600886689.

Cheli, F., Corradi, R., Sabbioni, E., Tomasini, G., 2011a. Wind tunnel tests on heavy road vehicles: Cross wind induced loads-part 1. J. Wind Eng. Ind. Aerodyn..

Cheli, F., Ripamonti, F., Sabbioni, E., Tomasini, G., 2011b. Wind tunnel tests on heavy road vehicles: Cross wind induced loads-part 2. J. Wind Eng. Ind. Aerodyn..

Cogotti, A., 2003. Generation of a controlled level of turbulence in the pininfarina wind tunnel for the measurement of unsteady aerodynamics and aeroacoustics. In: SAE World Congress & Exhibition. SAE International, http://dx.doi.org/10.4271/2003-01-0430.

Coleman, S., Baker, C., 1990. The Aerodynamics of Ground Vehicles in Cross Winds. University of Nottingham.

Coleman, S., Baker, C., 1994. An experimental study of the aerodynamic behaviour of high sided lorries in cross winds. J. Wind Eng. Ind. Aerodyn..

Deehan, M., Yaary, S., Longmire, K., Newcomb, L., Slocum, C., Sylvander, B., Allen, M., Arzayus, F., Decker, C., Oakes, S., Cromwell, M., Grasso, M., Murphy, T., Wielgus, J., Rosenlof, K., Schepel, K., Sims, C., Gillespie, A., Conran, J., Davis, S., 2025. 2024 NOAA Science Report. Technical Memorandum, NOAA, Silver Spring, MD, USA, http://dx.doi.org/10.25923/mh4h-pm52.

Dorigatti, F., Sterling, M., Rocchi, D., Belloli, M., Quinn, A., Baker, C., Ozkan, E., 2012. Wind tunnel measurements of crosswind loads on high sided vehicles over long span bridges. J. Wind Eng. Ind. Aerodyn..

European Committee for Standardization (CEN), 2019. EN 14067-6-2018+a1-2022 - railway applications — aerodynamics. Part 6: Requirements and test procedures for cross wind assessment.

European Environment Agency, 2024. European Climate Risk Assessment. EEA Report 01/2024, Publications Office of the European Union, Luxembourg.

Farrell, T., Miller, L.S., 2006. Development of a new boundary layer control technique for automotive wind tunnel testing. In: 44th AIAA Aerospace Sciences Meeting and Exhibit. American Institute of Aeronautics and Astronautics, http://dx.doi.org/10.2514/6.2006-356.

Han, Y., Hu, J., Cai, C.S., Chen, Z., Li, C., 2013. Experimental and numerical studies of aerodynamic forces on vehicles and bridges. Wind. Struct. 17 (2), 163–184. http://dx.doi.org/10.12989/was.2013.17.2.163.

He, X., Xu, Y.L., Guo, W., Li, Y., 2020. Wind tunnel tests on the aerodynamic characteristics of vehicles on highway bridges. J. Wind Eng. Ind. Aerodyn. 206, 104373. http://dx.doi.org/10.1016/j.jweia.2020.104373.

Heft, A.I., Indinger, T., Adams, N.A., 2012. Introduction of a new realistic generic car model for aerodynamic investigations. In: SAE Technical Paper Series, number 2012-01-0168 in SAE Technical Paper, SAE International. SAE International, http://dx.doi.org/10.4271/2012-01-0168.

Heft, A.I., Indinger, T., Adams, N., 2018. Experimental and numerical study of the DrivAer model aerodynamics. SAE Int. J. Passeng. Cars - Mech. Syst. 11 (2), 115–127. http://dx.doi.org/10.4271/2018-01-0741.

Hupertz, B., Chalupa, K., Krueger, L., Howard, K., Glueck, H.-D., Lewington, N., Chang, J.-H., Shin, Y.-s., 2021. On the aerodynamics of the notchback open cooling DrivAer: A detailed investigation of wind tunnel data for improved correlation and reference. SAE Int. J. Adv. Curr. Pr. Mobil. 3 (4), 1726–1747. http://dx.doi.org/10.4271/2021-01-0958, SAE WCX Digital Summit, SAE paper 2021-01-0958.

Intergovernmental Panel on Climate Change, 2023. Climate Change 2023: Synthesis Report. Contribution of Working Groups I, II and III to the Sixth Assessment Report of the Intergovernmental Panel on Climate Change. Technical Report, IPCC, Geneva, Switzerland, http://dx.doi.org/10.59327/IPCC/AR6-9789291691647.

International Organization for Standardization, 2010. Road vehicles — Sensitivity to lateral wind — Open-loop test method using wind generator input. Confirmed in 2023.

International Organization for Standardization, 2011. ISO 8855:2011 – Road vehicles — Vehicle dynamics and road-holding ability — Vocabulary. 2nd Edition, https://www.iso.org/standard/51180.html.

Ji, T., Li, Y., Wang, Y., Zhang, Y., Li, X., 2022. The impact of climate change on urban transportation resilience to compound extreme events: A review. Sustainability 14 (7), 3880. http://dx.doi.org/10.3390/su14073880.

Liu, X., Han, Y., Cai, C.S., Levitan, M., Nikitopoulos, D., 2016. Wind tunnel tests for mean wind loads on road vehicles. J. Wind Eng. Ind. Aerodyn. 150, 15–21. http://dx.doi.org/10.1016/j.jweia.2015.12.004.

Markolf, S.A., Hoehne, C., Fraser, A., Chester, M.V., Underwood, B.S., 2019. Transportation resilience to climate change and extreme weather events – beyond risk and robustness. Transp. Policy 74, 174–186. http://dx.doi.org/10.1016/j.tranpol.2018.11.003.

Passaggia, P.-Y., Mazellier, N., Kourta, A., 2021. Aerodynamic drag modification induced by free-stream turbulence effects on a simplified road vehicle. Phys. Fluids 33 (10), 105108. http://dx.doi.org/10.1063/5.0062232.

Sterling, M., Quinn, A., Hargreaves, D., Cheli, F., Sabbioni, E., Tomasini, G., Delaunay, D., Baker, C., Morvan, H., 2010. A comparison of different methods to evaluate the wind induced forces on a high sided lorry. J. Wind Eng. Ind. Aerodyn..

Stoll, D., Schoenleber, C., Wittmeier, F., Kuthada, T., Wiedemann, J., 2016. Investigation of aerodynamic drag in turbulent flow conditions. SAE Int. J. Passeng. Cars – Mech. Syst. http://dx.doi.org/10.4271/2016-01-1605.

Strangfeld, C., Wieser, D., Schmidt, H.-J., Woszidlo, R., Nayeri, C.N., Paschereit, C.O., 2013. Experimental study of baseline flow characteristics for the realistic car model DrivAer. SAE Int. J. Passeng. Cars - Mech. Syst. 6 (1), 117–127. http://dx.doi.org/10.4271/2013-01-1251.

Wieser, D., Nayeri, C.N., Paschereit, C.O., 2020. Wake structures and surface patterns of the DrivAer notchback car model under side wind conditions. Energies 13 (2), 320. http://dx.doi.org/10.3390/en13020320.

Wieser, D., Schmidt, H.-J., Müller, S., Strangfeld, C., Nayeri, C., Paschereit, C., 2014. Experimental comparison of the aerodynamic behavior of fastback and notchback DrivAer models. SAE Int. J. Passeng. Cars - Mech. Syst. 7 (2), 653–661. http://dx.doi.org/10.4271/2014-01-0613.

Wood, R., 2012. A review of Reynolds number effects on the aerodynamics of commercial ground vehicles. SAE Int. J. Commer. Veh. 5 (2), 628–639. http://dx.doi.org/10.4271/2012-01-2045.

Xiang, H., Guo, W., Cai, C.S., Han, Y., 2017. A wind tunnel test method on aerodynamic characteristics of moving vehicles under crosswinds. J. Wind Eng. Ind. Aerodyn. 171, 118–127. http://dx.doi.org/10.1016/j.jweia.2017.09.007.

Zhang, X., Li, Y., Chen, Z., Xu, Y.L., 2023. Wind tunnel investigations of crosswind loads for static road vehicles on wide bridge decks. J. Wind Eng. Ind. Aerodyn. 238, 105411. http://dx.doi.org/10.1016/j.jweia.2023.105411.

Zhu, L., Li, L., Xu, Y., Zhu, Q., 2012. Wind tunnel investigations of aerodynamic coefficients of road vehicles on bridge deck. J. Fluids Struct. 30, 35–50. http://dx.doi.org/10.1016/j.jfluidstructs.2011.09.002.